Geomechanics and Engineering, *Vol. 26, No. 1 (2021) 27-40*
https://doi.org/10.12989/gae.2021.26.1.027

Numerical modelling of the long-term effects of XCC piling in fine-grained soil

Fei Liu, Jiangtao Yi*, Junjie Dong and Hang Zhou

School of Civil Engineering, Chongqing University, No.83 Shabei Street, Chongqing, 400045, China

(Received February 27, 2021, Revised June 7, 2021, Accepted June 23, 2021)

Abstract. Although the development and utilization of X-section cast-in-place concrete (XCC) pile have been reported for some time, the long-term effects of XCC piling in fine-grained soil, in particular the set-up effects, have received little attention. This paper reports a coupled effective analysis of XCC piling using the dual-stage Eulerian-Lagrangian (DSEL) technique. The pile installation and subsequent soil consolidation was explicitly and consecutively modelled. The generation of excess pore pressure and alteration of stress states during the pile installation were explored. The distribution and magnitude of effective normal stress at pile/soil interface, in particular its evolution with time, were investigated. The influence of set-up effects on the XCC pile shaft resistance was assessed and quantified. It was found out, although the shaft resistances of both XCC and circular pile develops substantially with time, the consolidation in the wake of XCC pile installation can bring in more capacity enhancements and therefore practical benefits. The ultimate shaft resistance of XCC pile is 45% higher than that of the circular pile of the same cross-sectional area. Additionally, practical advice was given on how to optimize of the cross-sectional shape of XCC piles to take full advantage of set-up effects and achieve economical designs.

Keywords: effective normal stress; large deformation finite element analysis; set-up effect; shaft resistance; XCC pile

1. Introduction

As is well known, the bearing capacity of a pile foundation is jointly governed by its shaft and tip resistances (Poulos and Davis 1980). To increase the former i.e., shaft resistance component, one effective strategy is to optimize the pile cross-sectional shape so as to maximize the pile perimeter and therefore shaft surface (Lv *et al.* 2016, Lv and Zhang 2018). In the past decade, an innovative type of non-circular pile, i.e., the X-section cast-in-place concrete (XCC) pile, has been developed in China (Lv *et al.* 2012, Liu *et al.* 2014, Sun *et al.* 2017). Due to its higher shaft surface area and thereby more shaft resistance than ordinary piles, since its inception the XCC pile has been gaining increasing popularity, notably in the large-scale ground treatments of soft fine-grained soils for highway and railway constructions (Ding *et al.* 2020, Lv *et al.* 2014a, Zhou *et al.* 2018). As shown in Fig. 1, the cross-section of a typical XCC pile consists of four flat sides and four cambered sides. There are three geometrical parameters which dictate the cross-sectional shape, viz. open arc angle θ_0, diameter of circumcircle α and length of flat side b. The installation of a XCC pile consists of three consecutive steps: (a) penetrating the X-section pile mold fitted with conical shoe into the soft clay (see Fig. 2), (b) pouring concrete into the pile mold, (c) extracting the pile mold with XCC pile left in place. Clearly, the process of pile installation process invariably disturbs, displaces and squeezes the surrounding soil and alters the soil' stress states (Carter *et al.* 1979, Gavin *et al.* 2010, Peng *et al.* 2020, 2021), the case of saturated fine-grained soil, significant excess pore pressure build-up is expected. In the wake of pile installation, with the gradual dissipation of the excess pore pressure, effective stresses get progressively enhanced (Abu-Farsakh *et al.* 2015, Hyodo *et al.* 2019, Khanmohammadi and Fakharian 2017, Li *et al.* 2020, Liu *et al.* 2020). Amongst various stress components, the improvement of effective lateral/radial stress requires particular attention, as it explains the long-term development of pile shaft resistance or the set-up effect (Basu *et al.* 2014, De Chaunac and Holeyman 2017, Gong *et al.* 2020, Haque and Abu-Farsakh 2018, Karlsrud 2014, Wang *et al.* 2021).

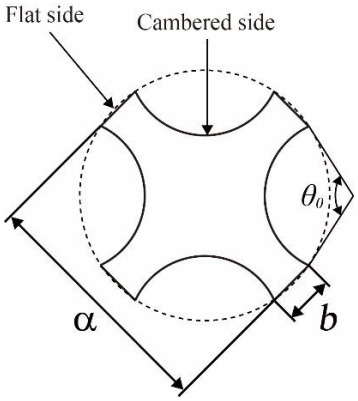

Fig.1 The cross-section of XCC pile

Since the beginning and particularly the first successful application (Lv *et al.* 2012), XCC pile has attracted much academic interest. To date, extensive research of various forms including experimental (Kong *et al.* 2015, Zhou *et al.*

*Corresponding author, Ph.D.
E-mail: yijt@foxmail.com

ISSN: 2005-307X (Print), 2092-6219 (Online)

(a)

(b)

Fig.2 Installation equipment: (a) X-section pile mold and (b) conical shoe (after Zhou *et al.* (2019))

2017), theoretical (Liu *et al.* 2014, Zhang *et al.* 2015) and numerical works (Lv *et al.* 2014b, Zhou *et al.* 2019) have been documented in the literature. Undoubtedly, these research outcomes contributed significantly to depending the understanding of load transfer mechanism, bearing capacity, static and dynamic responses, etc. of XCC piles. However, only a few of these studies alluded to the long-term behavior of XCC piles, out of which the numerical analyses concerning the set-up effect are remarkably scarce.

Although the finite element methods have been increasingly utilized to tackle extensive kinds of geotechnical problems (Azari *et al.* 2015, Lorenzo *et al.* 2016, Yi *et al.* 2012a, 2014, 2021), continually modelling the installation and subsequent consolidation of a XCC pile in saturated fine-grained soil remains a complicated task, which features a combination of large deformation, and generation and dissipation of excess pore pressure. What's more, the XCC pile, taking on an irregular cross-sectional shape, has a non-axisymmetric geometry, which renders it inapplicable to undertake the two-dimensional (2D) small-strain finite element calculations. For the latter, there are various effective techniques which can circumvent the limitation associated with element distortions, those including so-called Zipper technique (Yi *et al.* 2012a), Press-replace method (Lim *et al.* 2019), Cavity-expansion idealization (Rezania *et al.* 2017). The former, on the other hand, requires the involvement of three-dimensional (3D) large deformation finite element (LDFE) techniques. Recently, attempts have been successfully made by Zhou *et al.* (2019) who performed 3D finite element calculation of XCC pile installation using the Coupled Eulerian–Lagrangian (CEL) available in the commercial finite element program ABAQUS. Nonetheless, this reported analysis was essentially a total stress computation and provided no information on pore water pressure. As such, only the pile installation was modelled, with no consideration of post-installation consolidation as well as set-up effects. What's more, constrained by the total stress framework, the constitutive behavior of soils was there modelled as elastic-perfectly plastic material obeying Tresca yield criteria. In this regard, the 3D effective stress LDFE techniques such as those reported by Yi *et al.* (2012b, 2014), Ceccato *et al.* (2016, 2017) and Ullah *et al.* (2018) provided ideal technical resolutions in that they can continuously model both the XCC installation and consolidation, and realistically account for the sophisticated soil constitutive behavior.

This paper reports an effective stress analysis of XCC pile installation and consolidation using a 3D LDFE technique. The main objectives of the study are to 1) understand the generation and dissipation of excess pore pressure arising from XCC piling; 2) quantify the magnitude and establish the range of effective lateral stress variation during and after piling; 3) evaluate the set-up effects on XCC pile shaft resistance; 4) establish the significance of cross-sectional parameters on the long-term pile shaft capacity.

2. Numerical modelling methodology

2.1 Dual-stage Eulerian-Lagrangian technique

In this paper, an in-house developed effective-stress LDFE method i.e., dual-stage Eulerian-Lagrangian (DSEL) technique was used to continuously model the installation and consolidation of a single XCC pile. Since the details of this technique have been explained at length by Yi *et al.* (2012b, 2014), only a brief overview is provided herein. The whole package of DSEL program is comprised of three integral components or modules viz. the effective stress Eulerian module, the coupled-flow Lagrangian module and the mesh-to-mesh variable mapping module. The effective-stress Eulerian module is used to simulate the undrained installation of various foundations which features large deformation and strain without apparent dissipation of excess pore pressure, while the coupled-flow Lagrangian module is aimed at modelling the post-installation consolidation behavior of foundations which are characterized by a limited soil deformation and yet significant pore pressure dissipation. Thus, they are well suited to model the present installation and consolidation of a XCC pile, where the former and latter can be analyzed respectively by the Eulerian module in the first stage and Lagrangian module in the second stage. To bridge these two stages, the mesh-to-mesh variable mapping module has to be invoked, which seamlessly transfers the calculated results from the end of the first stage to the beginning of the second stage. In this study, the first stage analysis was conducted on the platform of ABAQUS/Explicit through an in-house developed subroutine, while the second stage was undertaken in ABAQUS/Standard. The solution mapping was undertaken outside the ABAQUS environment.

One thing should be clarified that, although the XCC pile is casted in place, its mold penetration, as described

earlier, bears close resemblance to the jacking of precast pile. The complex installation process of XCC pile was presently simplified as the jacking of X-shaped prefabricated pile. The mold extraction, in other words, was not explicitly considered in this study for simplicity.

2.2 Validation of the DSEL technique

Although several verifying examples for DSEL technique have been reported by Yi *et al.* (2012b, 2014, 2020), they were mainly conducted to validate its robustness in analyzing the installation and consolidation behavior of offshore spudcan foundations, rather than on-shore piles. For the latter objective, DSEL technique was applied in this section to simulate the centrifuge experiment of a jacked circular pile and the field test of a XCC pile reported in the literature.

2.2.1 Comparison with the centrifuge test by Li et al. (2017a, b, c)

Li *et al.* (2017a, b, c) reported a centrifuge experiment of a single pile installation and consolidation at the acceleration level of 50 g. The soil samples were remolded and reconstituted normally consolidated clayey soil, made of soft sediments taken from the fifth geological stratum in Shanghai city of China, the soil physical and mechanical properties being listed in Table.1. After high-g self-weight consolidation, the 10 mm-diameter circular model pile with a conical tip of a 60° apex angle was jacked at a constant penetration velocity of 50 mm/min into the soil layer until reaching a depth of 250 mm. The penetration velocities adopted for pile jacking were pre-calibrated such that they were adequately fast to ensure fully undrained penetration. After the completion of the pile jacking, pile was left in place for full consolidation. During pile jacking and soil consolidation, a pore pressure transducer was embedded behind the conical pile tip (i.e., at the pile shoulder) to keep track of pore pressure variation.

Numerical simulation with DSEL method was first carried out to replicate this centrifuge experiment, with soil constitutive behavior approximated by modified Cam-clay (MCC) model using soil parameters summarized in Table 1. According to Mahmoodzadeh *et al.* (2015), the MCC model is appropriate to capture the constitutive responses of normally to lightly over-consolidated fine-grained soils.

Fig. 3(a) shows the finite element model established for the first (Eulerian) stage. To facilitate the verification of the numerical model, the 3-D Eulerian analysis model shown in Fig. 3(a). Using the axisymmetry of the problem only a quadrant of a soil cube (i.e., a cuboid) was modeled. The diameter of the circular pile, D, is 0.5 m in prototype scale. The pile was discretized into 8-node Lagran-gian brick elements (C3D8R). Since the scope of this study is focused on the soil responses, thus the deformation of the pile itself was not consolidated and it was idealized as a rigid body, the movement of the rigid body can thus be conveniently controlled by simply prescribing boundary and load conditions with respect to its reference point.

The soil cuboid analyzed measures 20 m in depth, 10 m in width and 10 m in length, which is identical to the geometry and dimensions as those adopted in the centrifuge experiments. During pile installation, to cater for the large deformation of soil, the soil body was modelled as Eulerian domain and discretized into 8-node Eulerian brick elements (EC3D8R). Graded Eulerian meshes were adopted to balance the computational effort and accuracy, as shown in Fig. 3(a) where finer meshes were prescribed near the pile and increasingly coarser meshes were deployed towards the model boundaries. A 1m thick layer of void elements with zero strength and stiffness, was prescribed above the soil surface. That was necessary to allow material flow into this region during the installation process. During analysis, soil flows normal to the side and bottom surfaces of the cuboid were constrained, while tangential components were allowed. Following the preceding validation exercise, soil was approximated as a MCC material with parameters summarized in Table 1.

Table 1 Properties of the Shanghai soft soil (Li *et al.* 2017a, b, c)

Effective unit weight (γ')	8.75kN/m^3
Effective internal friction angle (φ')	30°
Interface friction angle （ δ ）	16.5°
Slope of isotropic virgin compression line (λ)	0.11
Slope of swelling/recompression line (κ)	0.02
Coefficient of earth pressure at test (K_0)	0.55
Effective Poisson's ratio, υ	0.28
Coefficient of permeability (k)	2.67×10^{-9} m/s
Initial void ratio (e_{ini}) at p'=1kPa	0.98

The soil-pile interface was explicitly modelled using a general contact algorithm provided by ABAQUS V6.14 (Dassault 2014), which allows for large sliding and separation between pile and soil surfaces. No account was given to the contact friction, where soil-pile interface was assumed to be fully smooth. Such simplification was made mainly because total stress Coulomb friction formulation is adopted in ABAQUS/Explicit which would overestimate of the interfacial friction as the latter by right should be calculated in terms of effective stress.

The initial stress condition prior to pile installation was assumed to follow the K_0 stress condition, which is a rational approximation of in-situ undisturbed soil stress condition. After Jaky (1948), the initial lateral stress coefficient K_0 is set to 0.55 for the clay. The pile initially suspended above soil was then continually jacked into the soil at a constant rate of 0.1m/s until reaching depth of 12.5 m, the choice of penetration rate was not critical as long as it was not too fast to bring in dynamic effect (Tho *et al.* 2012).

After the first calculation stage, the deformed geometry of soil was extracted from Eulerian model (Fig. 3(b)), which was then used to define the initial geometry of the Lagrangian model (Fig. 3(c)) for the second stage. The Lagrangian model was then discretized into 8-noded brick elements with both displacement and pore-pressure degrees-of-freedom (C3D8P), compatible with coupled pore pressure analysis. Various solution variables were then

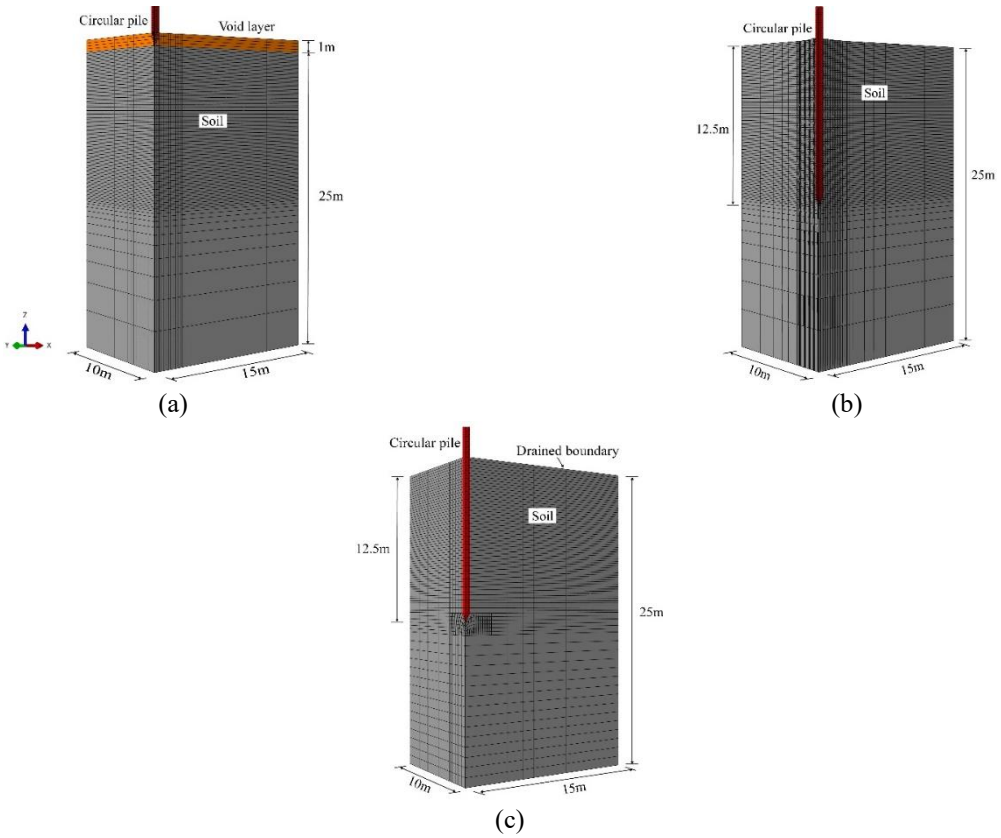

Fig. 3 DSEL finite element models at different calculation stages: (a) undeformed Eulerian model, (b) deformed Eulerian model and (c) Lagrangian model

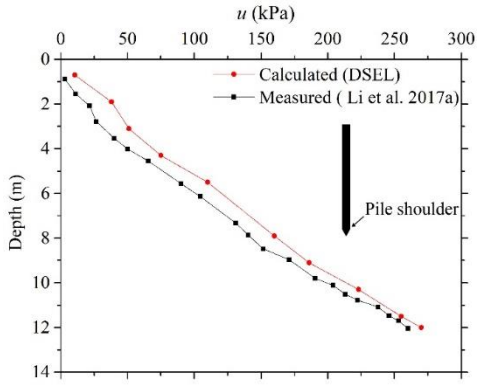

Fig. 4 Computed and measured pore pressure profile at the pile shoulder position

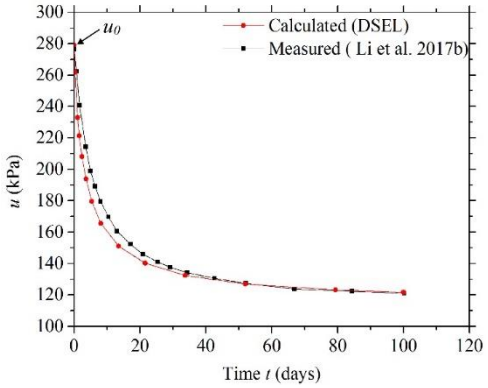

Fig. 5 Computed and measured pore pressure decay following pile installation at the pile shoulder position.

transferred from the end of Eulerian analysis to the beginning of Lagrangian analysis via the mesh-to-mesh mapping algorithm. Thereafter, the coupled flow analysis with free drainage assumed at the top soil surface was undertaken to model the soil consolidation behavior. During this stage, the pile was held in place without settlement or tilting, while excess pore pressure dissipated and soil settled.

Fig. 4 presents the computed and experimentally measured pore pressure "*u*" at the shoulder position while pile was being continually jacked to different depths. (These computational results are extracted from the first/Eulerian calculation stage.) Note that all results are herein and hereafter interpreted at prototype scale. It is readily noted from Fig. 4 that both computed and measured pore pressures increased approximately linearly with penetration depths. Such variation trends are agreeable with the linear strength profiles of normally consolidated soils. The DSEL analysis results tended to somewhat over-predict the experimental ones. These insignificant over-predictions may be attributable to that the soil strength gradient reported in the experiment was slightly lower than that included in DSEL analysis. (Although the soil sample in the experiment was subject to high-g self-weight consolidation for up to 12 hours, it did not reach 100% consolidation degree (Li *et al.* 2017a, 2017b, 2017c). Notwithstanding the above, reasonable accordance was achieved between the DSEL analysis and the centrifuge test results.

Fig. 5 presents the calculated and measured time histories of pore pressure decay, i.e., dissipation curves,

again at the pile shoulder. (These computational results are taken from the second/ Lagrangian calculation stage.) What can be first noted from this graph is the initial pore pressure values, i.e., "u_0" as marked in the graph, is close to u computed at the final depth of Fig.4. This makes sense since the initial stress and pore pressure values of the Lagrangian stage are mapped from the Eulerian stage. The subsequent dissipation curves from experimental and numerical data exhibit satisfactory match, which clearly verify the robustness of DSEL technique when applied to consecutively analyzing the pile installation and consolidation.

2.2.2 Comparison with the field test reported in Kong et al. (2015)

Kong *et al.* (2015) reported a field experiment of XCC piling, conducted in deltaic deposits, located in the north-east suburb of Nanjing. The three parameters controlling the shape of the XCC pile cross-section i.e., the open arc angle θ_0 , diameter of circumcircle α and length of flat side b are 611 mm, 120 mm and 180 mmm respectively. As shown in Fig. 6, multiple sensors were used to monitor changes in pore pressure and radial total stress. These sensors were located in two vertical polar planes (θ = 0° and θ = 45°), and placed at three radial distances (1m, 2m, and 3.5m) and a 6m depth. The final penetration depth of XCC pile is 12m. It should be noted that the measurements were recorded directly during the XCC pile installation, which is consistent with the assumption of undrained conditions. The experimental site was comprised mainly of clayey soil with low plasticity, and the soil strength increased from approximately 45 kPa at 0.9 m to 99 kPa at 14.8m based on cone penetration test results. As details with respect to these field experiments are furnished in Kong *et al.* (2015), they are not further elaborated on. Instead, attention is directed to the comparison between measured and calculated results.

To facilitate direct comparison with field test data, the penetration process of the XCC pile is simulated using the three-dimensional model in shown in Fig. 6. In order to save computational time only a quarter of the simulation model is discretized. The XCC pile is a rigid boby such that it does not experience any deformation during analysis. The penetration stage of the XCC pile is modelled displacement-controlled with a velocity of 0.1 m/s.

The overall dimensional of the Eurlerian domains for soil comprises a 24 m in depth, 10 m in width and 10 m in length. During analysis, the meshes and boundary conditions and were coincident with those in Section 2.2.1. The top 1m of the Eulerian domain is modeled material-free, this is necessary to allow soil material flow into this region during the XCC pile penetration. The soil and pile domains were discretized into 8-noded Eulerian brick elements (EC3D8R) and 8-noded Lagran-gian brick elements (C3D8R) respectively.

Before the XCC pile penetration, the geostatic stress was imposed in a predefined step to consider the soil self-weight.

In consistent with the finite element model established for the first (Eulerian) stage mentioned in Section 2.2.1, the friction between soil and pile was ignored for simplification. Following the preceding validation exercise, soil was approximated as a MCC material with parameters summarized in Table 1.

The computed and measured radial variation of the normalized maximum radial stress increment ($\Delta\sigma_{r,max}$ / σ'_{vo}) over the entire course of XCC pile installation, at the

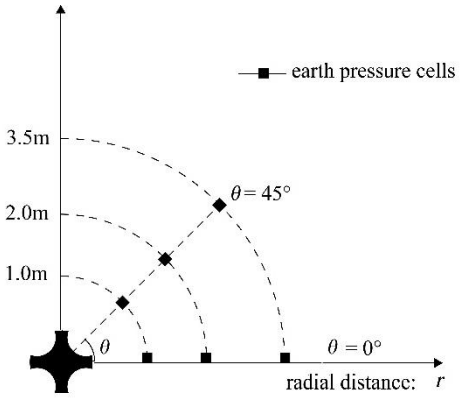

Fig. 6 A schematic diagram of the XCC pile field test with instrumentation layout (adapted from Kong *et al.* (2015)). Polar angle θ is defined in a cylindrical coordinate system with its vertical axis coincidental with the pile axis

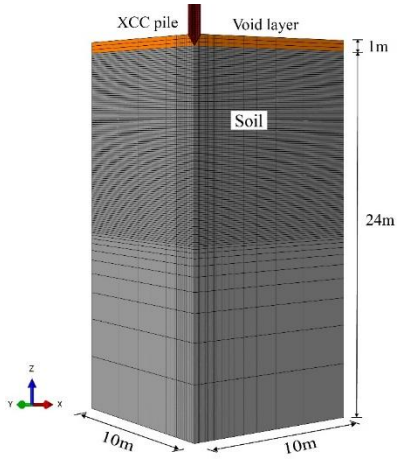

Fig. 7 Eulerian model for XCC pile penetration

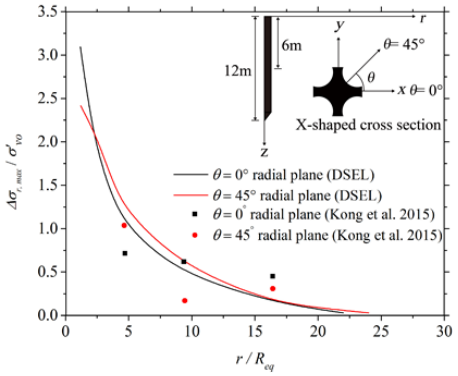

Fig. 8 Computed and measured radial variation of the normalized maximum radial stress increment ($\Delta\sigma_{r,max}$ / σ'_{vo}) over the entire course of XCC pile installation, at the depth of 6 m

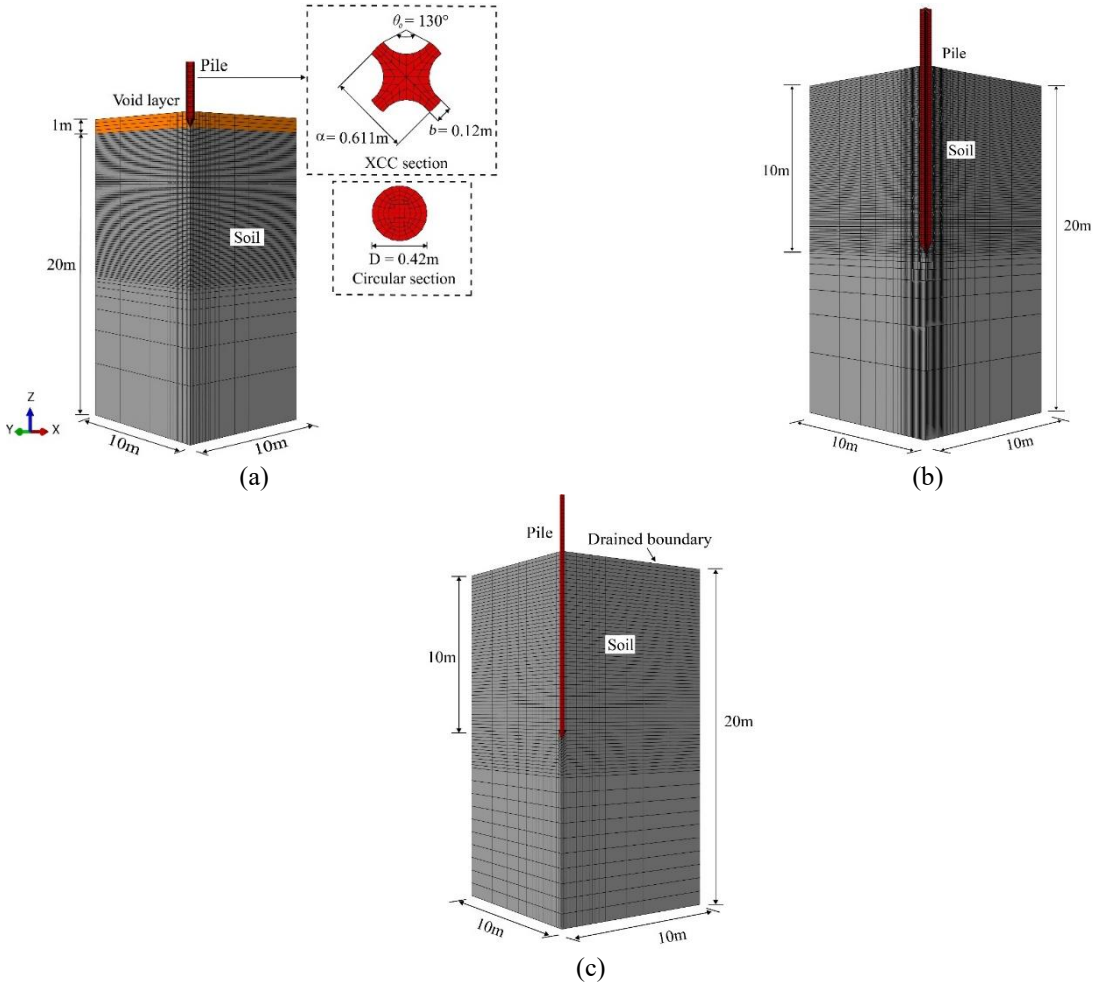

Fig. 9 Finite element model: (a) Eulerian finite element model (undeformed), (b) Eulerian finite element model (deformed) and (c) Lagrangia finite element model

depth of 6 m, is plotted in Fig. 8. $\sigma_{r,max}$ and σ'_{vo} are herein the maximum change in radial total stress and in-situ effective vertical stress, respectively. The radial distance r is normalized by the equivalent radius R_{eq}, where $R_{eq}=\sqrt{(\frac{A_x}{\pi})}$ and A_x is the pile cross-sectional area. It is clear from Fig. 8 that the computed results match reasonably with the field measurements. This thus lends further confidence to the accuracy and reliability of DSEL analysis results.

2.3 Finite element models

This section presents the finite element models and numerical procedure built to simulate the penetration and consolidation of the XCC pile and circular pile, which generate the major results and findings of this study. Since the numerical model and boundary conditions adopted herein are similar to those in validation (Section 2.2), the latter of which have been described in detail previous, they are not expanded on herein for avoiding repetition. Only the salient points are presented in this section.

Fig. 9(a) shows the pile and soil models established in the first/Eulerian stage, which models the large deformation, undrained penetration of pile. By virtue of symmetry, only a quadrant of a soil model was employed to improve computational efficiency. The cross-sectional geometry parameters of the XCC pile in numerical model are the same as that of field experimental pile in Kong *et al.* (2015) (2α = 610 mm, 2b = 240 mm, θ_0= 130°), having a total cross-sectional area of A_x = 0.14 m^2 and a perimeter of C_x = 2.18 m. The diameter of the circular pile, D, is 0.21 m, giving an identical cross-sectional area. Since the scope of this study is limited to the soil responses, particularly the set-up, to the pile installation, the deformation of the XCC pile itself was not considered and it was idealized as a rigid body using 8-noded Lagran-gian brick elements (C3D8R). The continuous penetration process was controlled by applying a constant velocity of 0.1 m/s to the reference point of the pile.

Right underneath the pile tip lies a cubic soil model, 20m in height by 10 m in width by 10 m in thickness, the dimensional and the Eulerian mesh are shown in Fig. 9(a). The soil domain consist of two layers, i.e., the soil layer and the void layer where void elements was prescribed with no material filled in. This was warranted to cater for soil heave above the initial soil surface during the pile penetration. During the Eulerian calculation, soil flow in and out of side and bottom surfaces of the cuboid is forbidden to prevent

material loss. The soil is meshed as 8-noded Eulerian brick elements (EC3D8R). The constitutive behaviour of soil was modelled by the modified Cam-clay (MCC) model with parameters listed in Table 1.

The pile-soil interaction was modelled using the surface-based Eulerian-Lagrangian contact formulation which allows for large arbitrary sliding between pile and soil surfaces. The soil-pile interface was assumed to be fully smooth mainly for simplicity.

The initial *K0* stress condition was imposed into the soil domain. The specified initial soil stress condition should match a calculation based on the self-weight of the soil material. During the calculation, the pile initially located above the soil surface was continually penetration into the soil at a constant rate of 0.1 m/s until reaching depth of 10 m.

After completing the calculation of the first/Eulerian stage, the deformed geometry of the soil domain is extracted from the Eulerian model (Fig. 9(b)), which is applied to as the initial geometry of the Lagrangian model (Fig. 9(c)) for the second calculation stage. Various solution results include effective stress components, void ratio and pore pressure were then transferred from the Eulerian meshed into the Lagrangian meshes. The free drainage condition was prescribed at the soil surface. Thereafter, the coupled flow analysis was performed to calculate the post-installation consolidation responses.

3. Results and discussions

This section is going to present the computational results of XCC installation and consolidation, together with pertinent interpretations and discussions. Before moving to the details, it may be more convenient to give an overview. The contents of this section are divided into three parts to facilitate reading. The first part is intended to shed some lights on the installation behaviors of XCC piling in terms mainly of excess pore pressure and effective radial stress. The second part is aimed at ascertaining the long-term effects of XCC piling, with emphases on the fully equalized stress conditions and set-up effects on pile shaft resistance. A comprehensive parametric study is presented in the third part, with a view to establishing an optimal shape of cross section which can maximize the set-up effects on pile shaft resistance.

3.1 Pile installation: short-term pore pressure and stresses

Fig. 10 plots the contours of pore pressures (u) by the end of XCC Pile driving (EOD) at $\theta = 0°$ and $\theta = 45°$ planes of soil domain, based on calculation results of the first stage (Eulerain) analysis. The hydrostatic pore pressure (u_0), denoted by dash lines, is also depicted in Fig 10 for comparison. It is clear from Fig 10 that significant pore pressure increases are located in the vicinity of XCC pile shaft and tip. The high pore pressure concentrated these areas is a result of accumulation of excess pore pressure generated during the continuous penetration of pile. Clearly,

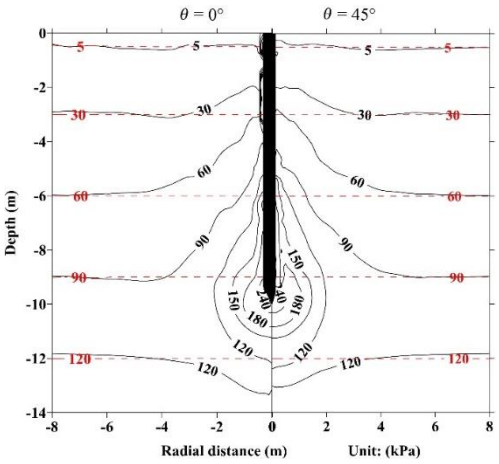

Fig.10 Distribution of pore pressures (u) in $\theta = 0°$ (left) and 45° (right) radial planes at the end of XCC pile installation

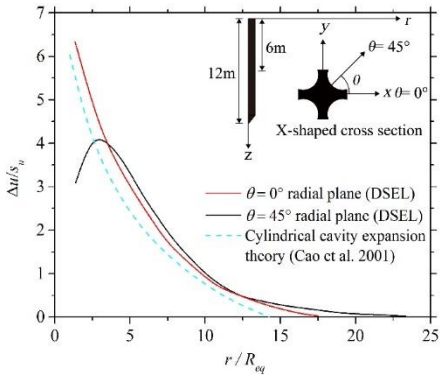

Fig. 11 Radial distribution of normalized excess pore pressures ($\Delta u/s_u$) at the end of XCC pile installation, at the depth of 9 m

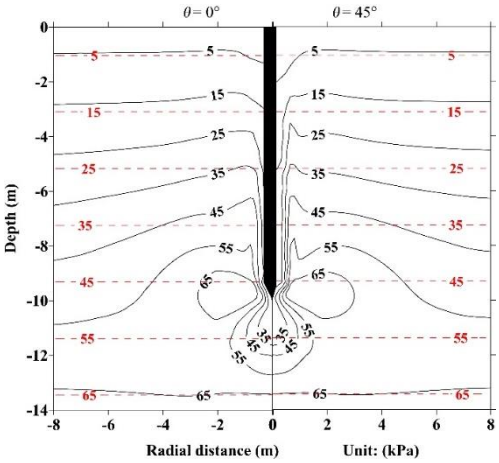

Fig. 12 Distribution of radial effective stress (σ_r') in $\theta =$ 0° (left) and 45° (right) radial planes at the end of XCC pile installation

the contours in the left (θ = 0°) and right (θ = 45°) hand sides are not symmetrical, as a result of non-symmetrical pile cross-section and thus asymmetrical longitudinal pile profiles (see Fig. 10). To further illustrate this point, Fig. 11 presents the radial distribution of $\Delta u/s_u$ at one representative

depth of soil domain (9m) extracted from $\theta = 0°$ and $\theta = 45°$ radial planes, where $\Delta u/s_u$ is the excess pore pressure Δu normalized by its corresponding in-situ shear strength s_u. What can be first noted from Fig. 11 is that $\Delta u/s_u \sim r/R_{eq}$ curves associated with $\theta = 0°$ radial plane and $\theta = 45°$ radial plane display dissimilar characteristics. For the former, $\Delta u/s_u$ decays monotonically with r/R_{eq} where its maximum value is located right at the pile wall. The latter, on the other hand, it peaks when $r \approx 2.5R_{eq}$. This phenomenon can be attributable to the shear dilatation which has been long recognized to generate negative Δu (Basu *et al.* 2014). Owing to its irregular cross-sectional shape, the significance of shearing is not uniform across the perimeter and throughout the depth. It is noted to be the most significant at the shoulder of the $\theta = 45°$ radial plane (i.e., the middle of cambered segment). As a consequence, $\Delta u/s_u$ registers its maximum not right at the pile wall, instead at some distance away from it.

For comparison sake, the prediction of Δu from the cylindrical cavity expansion theory of Cao *et al.* (2001) are also superimposed in Fig. 11. Note that the cavity expansion calculation was presently made using the equivalent radius R_{eq} since the irregular cross-section could not be factored into calculation. It can be clearly seen that there is apparent discrepancy between cavity expansion solutions and DSEL results, notably when comparison is made in $\theta = 45°$ radial plane. The reasons for such discrepancy are likely twofold: ignorance of vertical shearing (Li *et al.* 2021, Rosti 2016, Silvestri *et al.* 2012) and disregard of irregular cross-sectional shape when the cavity expansion theory is employed to analyze the XCC pile installation.

The effective radial stress σ_r' contour lines at EOD within $\theta = 0°$ and $\theta = 45°$ planes of soil domain are depicted in Fig. 12. (Note that the radial directions in these planes coincide with normal directions of pile shaft. As such, σ_r' is interchangeable with effective normal stress σ'_n in these contexts.) Also superimposed in the graph is the in situ effective lateral earth pressure (σ'_{h0}), represented by dash lines. From this plot, it is noted that the distribution of the σ_r' within the $\theta = 0°$ and $\theta = 45°$ planes are much alike. Generally, the radial stresses rise over the initial stresses in response to the radial densification caused by pile installation. Nonetheless, there exist apparent and dramatic decreases of σ_r' when it come to the close proximity of pile shaft. Such dips can be explained by that soils lying right within and close to the penetration path of pile have been dragged down by the passage of advancing pile. Relatively, the dips are more severe in the $\theta = 45°$ plane (the right hand side of Fig. 12). This is consistent with the preceding observation that shearing is more significant in this plane.

3.2 Post-installation consolidation: stress build-up and set-up

From this section onwards, efforts will be directed towards exploring the post-installation behavior of soils in the wake of the XCC piling. In this section, particular emphasis is placed on ascertaining the effects of consolidation on the soil stress and shaft resistance.

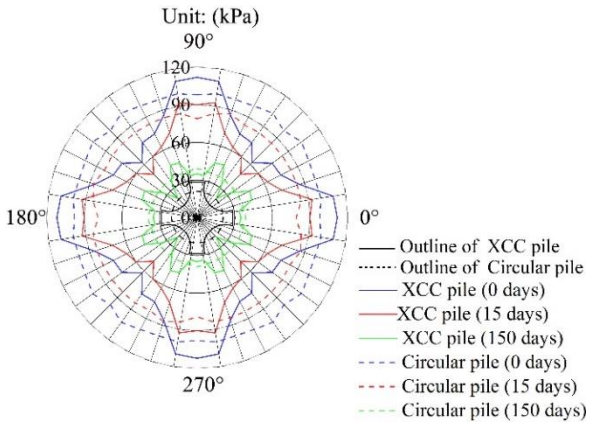

Fig.13 Distribution of the effective normal stress (σ'_n) at the pile surface at different time instants (0, 15, 150days) subsequent to XCC pile installation at the depth of 9 m

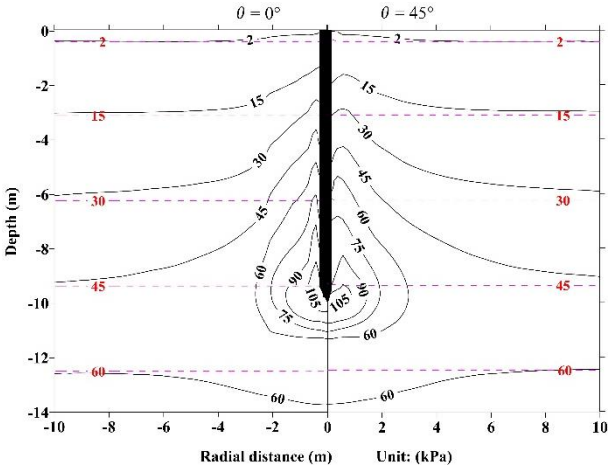

Fig. 14 Distribution of the effective radial stress (σ_r') in θ = 0° (left) and 45° (right) radial planes at the end of consolidation

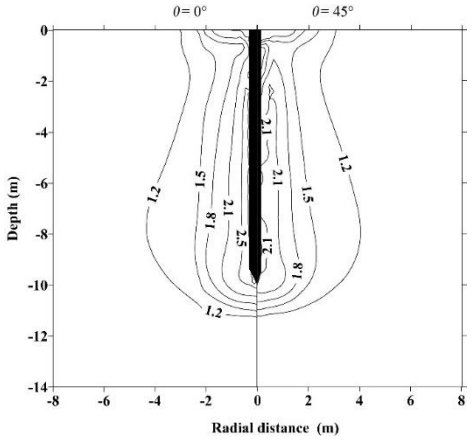

Fig. 15 Distribution of the stress improvement ratio (R_s) in θ = 0° (left) and 45° (right) radial planes at the end of consolidation

3.2.1 Stress build-up

Fig. 13 illustrates the distribution of effective normal stress σ'_n at the pile/soil interface at the mentioned depth (9m) over the course of post-installation consolidation.

Three typical time instances (namely 0, 15, 150days) following the XCC pile installation were selected, which produced short-term (undrained), intermediate (partial drained), long-term (full drained) stress states. For comparison, a companion analysis was performed with the area/volume-equivalent circular pile having a radius of R_{eq}. Its analysis results are also superimposed in Fig. 13. From this graph, three major observations can be made: 1) σ'_n of both XCC and circular pile develops apparently with time. By the end of consolidation (EOC), the long-term stresses nearly triple the short-time ones. 2) The geometrical shape of pile cross-section (i.e. X-shape or circular shape) is of marked relevance to the distribution of σ'_n. Unlike the circular pile where σ'_n is uniformly distributed, σ'_n of XCC pile is apparently concentrated on the flat sides. Such stress concentration is probably explained by the combined influence of radial squeezing on the flat side and downward dragging on the cambered side described earlier. These two effects in combination lead to severe stress concertation as noted above. 3) σ'_n of circular pile is bounded by the maximum (on the flat sides) and minimum (on the cambered sides) of XCC pile. In fact, the average effective normal stress of circular pile is slightly larger than that of XCC pile, as to be discussed at length later on.

Fig. 14 depicts σ'_r contour lines at EOC within θ = 0° and θ = 45° planes of soil domain. It is clear that σ'_r increasingly rises up compared with the σ'_{h0} when it approaches the pile wall. In particular, such stress build-up is more notable in areas adjacent to pile tip and shoulder (e.g. increasing from approximately 45kPa to 105kPa at the pile shoulder). Besides, the magnitudes of σ'_r next to XCC pile wall in the θ = 0° plane are somewhat higher than those in the θ = 45° plane, although the influence zone of the latter seems larger. The reasons for this phenomenon have been earlier explained.

Practically, the enhancement in effective radial stresses arising from consolidation can be quantified by a quantity called the stress improvement ratio R_s:

$$R_s = \frac{\sigma'_r}{\sigma'_{h0}} \quad (1)$$

Fig. 15 illustrates the calculated R_s at EOC of XCC pile. Clearly, R_s register apparent increases in wide areas surrounding the XCC pile. The area with discernable enhancement of R_s (R_s > 1.2) extends horizontally to about 4m from the XCC pile shaft and vertically to nearly 2m below the XCC pile tip. In particular, R_s close to the pile shaft and tip, is as large as 2.5 at the θ = 0° plane and 2.1 at the θ = 45° plane. That is to say, the effective radial or normal stresses at the pile shaft gain 110% - 150% increments over the in-situ stress.

3.2.2 Set-up effects on XCC pile shaft resistance

In the design of piles foundation, one extensively used method to estimate the friction on the soil-pile interface (f_s) in cohesive soil is the effective stress approach, more commonly known as "β-method":

$$f_s = \sigma'_n \tan\delta = K_f \sigma'_{v0} \tan\delta \quad (2)$$

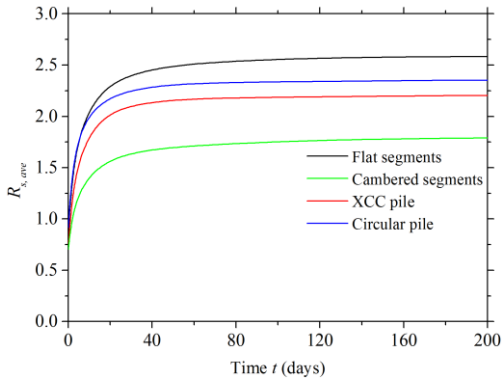

Fig. 16 Development of the average R_s ($R_{s,ave}$) with time at the depth of 9 m

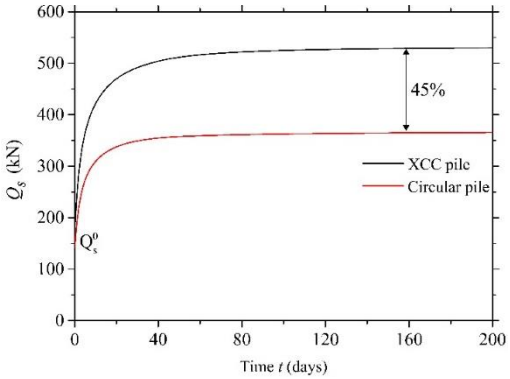

Fig. 17 Development of the pile shaft resistance Q_s with time

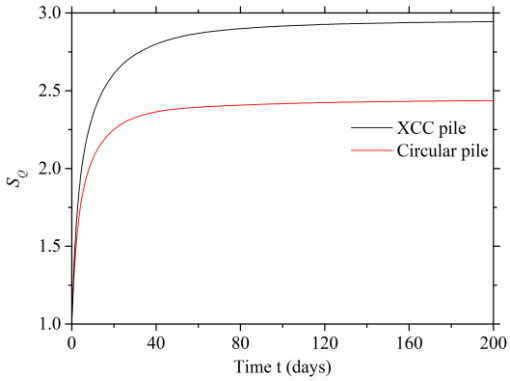

Fig. 18 Development of the set-up ratio S_Q with consolidation time

where δ is interface friction angle between the pile surface and soil; K_f is the lateral earth pressure coefficient over the pile shaft surface. Therefore, the proper estimation of f_s depends largely on the determination of K_f. In principle, K_f should reflect the stress enhancement arising from the post-installation consolidation and thus is a function of time. However, even in the latest design codes (API 2014), the set-up effect is commonly ignored, where K_f is usually taken as the in-situ lateral earth pressure coefficient K_0, i.e., $K_f = K_0$. This occurs at least partly because of lack of sound knowledge of updated lateral earth pressure coefficient at the end of consolidation.

As explained in Eq. (1), the stress build-up has been

quantified by R_s. To incorporate the set-up effect into shaft friction calculation, the β-method can be re-expressed as follows:

$$f_s = R_s\sigma'_{ho}\tan\delta = R_sK_0\sigma'_{vo}\tan\delta \quad (3)$$

As can be readily inferred from Fig. 15, R_s changes greatly around the perimeter of the cross-section of XCC pile. Therefore, an average value $R_{s,ave}$ is practically more meaningful and representative. In this study, $R_{s,ave}$ is obtained from the line integral:

$$R_{s,ave} = \frac{1}{L}\int_0^L R_s \ dl \quad (4)$$

where L is the integral distance. When L is the length of the entire perimeter, $R_{s,ave}$ produces the average value along the entire perimeter. On the other hand, when L is limited to length of flat or cambered segments, $R_{s,ave}$ gives the average value on the flat or camber segments of the XCC pile. Fig. 16 shows the historical development of $R_{s,ave}$ over the course of consolidation at the depth of 9m. It simultaneously presents $R_{s,ave}$ of XCC pile (along the entire perimeter), flat segments and cambered segments. Besides, for comparison purpose, $R_{s,ave}$ corresponding to the circular pile is also included in the same diagram, which are calculated based on results of the aforementioned companion analysis. From Fig. 16, there are a few observations worthy of highlighting 1) $R_{s,ave}$ is a time-dependent variable whether XCC or circular piles. It increases rapidly at the early stage (t < 20days). Thereafter, the rate of increase gradually declines with time. Approximately 60 days after XCC pile installation, $R_{s,ave}$ tends to stabilize signifying the completion of post-installation consolidation or EOC. 2) Whilst the time development trends of $R_{s,ave}$ on the flat and camber segments are much alike, the former is clearly larger than the latter (by as much as 50%) throughout the consolidation. This is plausible and in line with preceding observation in Fig. 13, where stress concentration at flat sides has been noted. 3) It turns out that $R_{s,ave}$ of the XCC pile is somewhat lower than $R_{s,ave}$ of the circular pile. This implies the adoption of an X-shaped pile cross-section tend to lower down the average stresses likely due to the stress concentration described above.

With the determined $R_{s,ave}$, the friction accumulated from the ground surface to depth Z, Q_z can then be conveniently estimated as follows:

$$Q_z = CK_0\tan\delta\int_0^Z R_{s,ave}\ \sigma'_{vo}dz \quad (5)$$

where C donates the circumference of the pile cross-section. When Z is equal to the entire shaft length L_{shaft}, Q_z corresponds to the pile shaft resistance Q_s. The calculated Q_s of both the XCC and circular piles are plotted in Fig. 17. Unsurprisingly, Q_s~ t curves bear high resemblance to preceding $R_{s,ave}$ ~ t curves of Fig. 16. With the development of time, Q_s progressively develops increasing from short-term undrained capacity Q_s^0 through to the long-term/ultimate shaft capacity Q_s^∞. Interestingly, Q_s of XCC pile is significantly higher than that of its corresponding circular pile, as shown in the graph. The discrepancy in Q_s^0 of these two piles is 22%, whereas Q_s^∞ differs by as much as 45%. Considering the earlier observation that $R_{s,ave}$ of XCC pile is slightly lower than that of the circular pile, this means the beneficial effects arising from much greater circumference of XCC pile clearly eclipse the influence of the lower stress improvement ratio $R_{s,ave}$. As a whole, XCC pile can mobilize much higher shaft resistance than its area/volume-equivalent circular pile in both short- (Q_s^0) and long- (Q_s^∞) term capacities.

To further quantify the set-up effect, a term called "set-up" ratio in shaft resistance S_Q is defined as follows:

$$S_Q = Q_s \ / \ Q_s^0 \quad (6)$$

These data shown in Fig. 17 were then further processed to infer S_Q for both XCC and circular piles, which are plotted against time t in Fig. 18. It is clear that both S_Q of the XCC and circular piles exhibits apparent and significant rises with time. That is to say, the set-up effects in shaft capacity is of significance regardless of pile types. By comparison with circular pile, the set-up effect of XCC pile is remarkably more pronounced. For instance, S_Q at EOC reach up to 2.9 or so, whereas it approaches 2.3 in the circular pile case. In other words, the long-term XCC pile shaft capacity is as much as 2.9 times its short-term one. This highlights the need to take account of set-up effects notably for XCC pile design, which can bring in more practical benefits than the conventional circular piles.

3.3 Parametric study: Optimizing the cross-sectional shape of a XCC pile

As explained above, the cross-sectional shape of a XCC pile is dictated by the three geometrical parameters, open arc angle θ_0, diameter of circumcircle a and length of flat side b (see Fig. 1). Endeavors are made in this section to optimize the cross-sectional shape by manipulating these three parameters so as to take full advantage of set-up effects on the shaft resistance. From economical viewpoint, an optimal cross-section shape should be the one that can mobilize the biggest shaft resistance for a given cross-section area/volume. Thus, a material efficiency coefficient C_m is herein defined as the ultimate shaft resistance per unit volume, $C_m = Q_s^\infty/V$. This quantity will be assessed and discussed throughout this section as the indicator of "optimization".

Note that the computational case described in the earlier sections with cross-sectional configuration (i.e., θ_0 = 130°, a = 0.611 m and b = 0.12 m) serves as the "base case" in this parametric study. While maintaining other parameters unchanged, one parameter is selected and varied to explore its influence in each of the following subsections.

3.3.1 Influence of θ_0

The attention is first paid to θ_0. As illustrated in Fig. 19, seven different arc angles (namely θ_0 = 30°, 60°, 90°, 110°, 130°, 150° and 180°) was studied for a = 0.611 m and b = 0.12 m. Physically, a bigger θ_0 produces a longer cambered segment with greater curvature when the

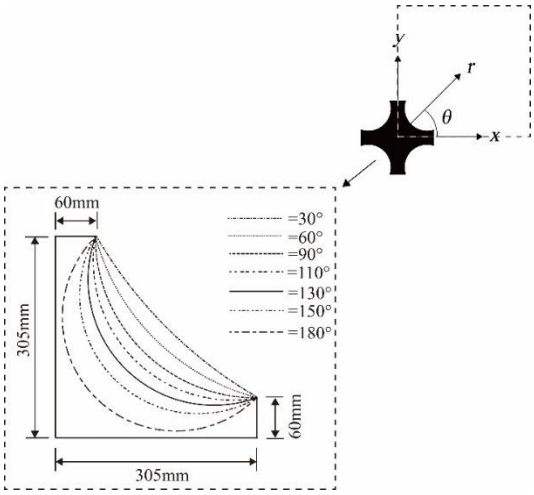

Fig. 19 Schematic illustration of the relevance of θ_0 to XCC pile cross-sectional shape (a quadrant). (a = 611 mm, b = 120 mm)

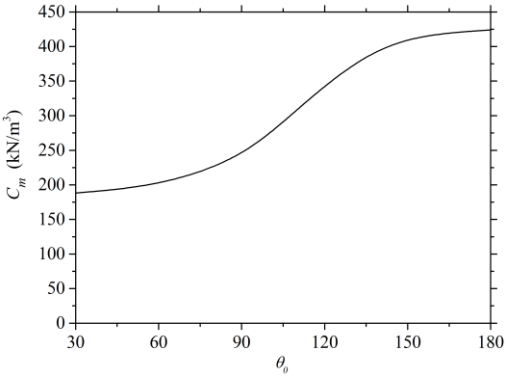

Fig. 20 Variation of material efficiency coefficient (C_m) with θ_0

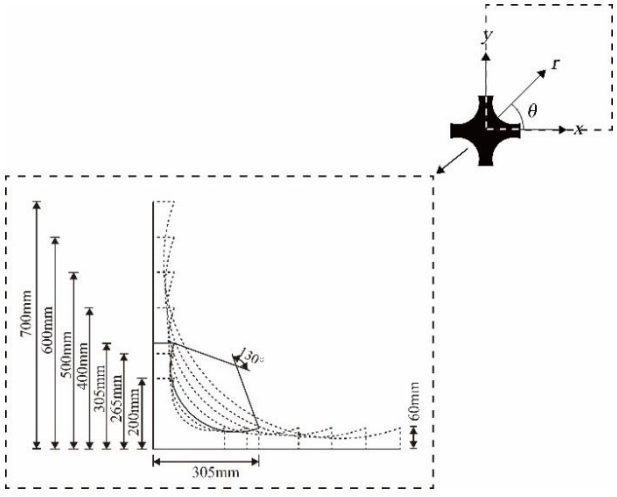

Fig. 21 Schematic illustration of the relevance of a to XCC pile cross-sectional shape (a quadrant). (θ_0 = 130°, b =120 mm)

diameter of circumcircle and length of flat segment (i.e., a and b) are maintained. Consequently, the area of X-shaped cross-section shrinks with the increasing θ_0. Also, varying θ_0 leads to the redistribution of σ'_n surrounding the XCC

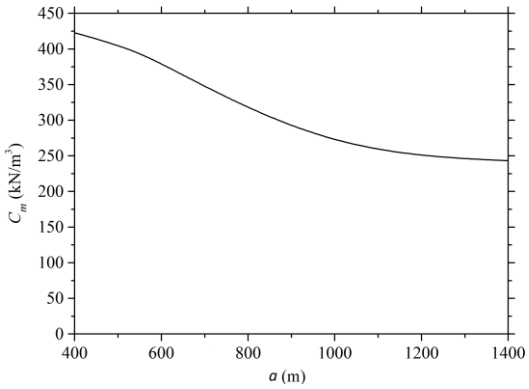

Fig. 22 Variation of material efficiency coefficient (C_m) with a

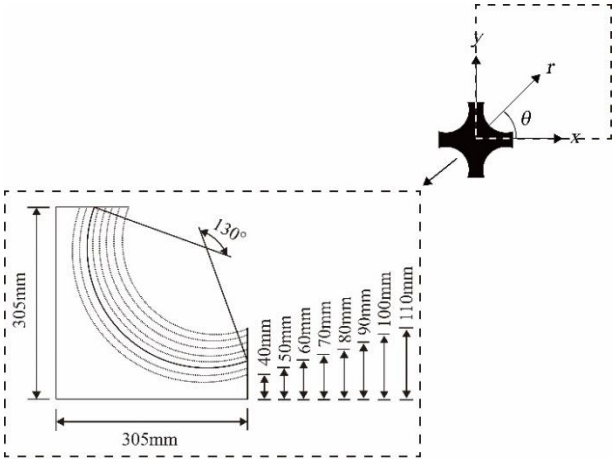

Fig. 23 Schematic illustration of the relevance of b to XCC pile cross-sectional shape (a quadrant). (θ_0 =130°, a = 611 mm)

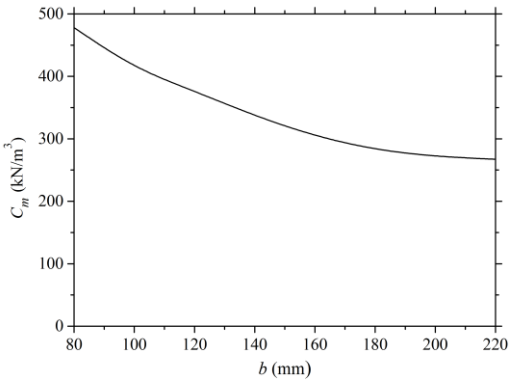

Fig. 24 Variation of material efficiency coefficient (C_m) with b

pile, thereby influencing the ultimate shaft resistance of XCC pile. As a result, θ_0 is relevant to C_m, as demonstrated in Fig. 20. It is clearly from this graph that C_m generally increases with the increase in θ_0. The influence of θ_0 is most appreciable within the range between 60° and 150°. By increasing θ_0 from 60° to 150°, C_m is more than doubled. On the other hand, C_m is nearly immune to θ_0 when the latter becomes less than 60° or greater than 150°. As explained above, the cross-sectional area reduces with increasing θ_0. An unduly large θ_0 may render the pile shaft too slender

which is thus susceptible to structure problems such as buckling. Given C_m is insensitive to θ_0 when $\theta_0 > 150°$, it is thus recommended an optimal value of θ_0 of 150°, which may best balance the material efficiency and structural stability.

3.3.2 Influence of a

Similarly, seven different diameters of circumcircle a falling in the range 400 mm to 1400 mm, which is coincidental with the practical range recommend by the design code, are investigated while θ_0 = 130° and b = 120 mm. As depicted in Fig. 21, varying a alone leads to the changes in both arc length and curvature of cambered segment. A larger a produces an elongated arc length and vice versa. Unlike the preceding case of θ_0, the elongation of arc is not accompanied by the increase in curvature in this case. Instead, the concave becomes less curved, with simultaneous increase in the cross-sectional area.

The significance of parameter a to C_m is illustrated in Fig. 22. Generally, C_m declines as a increases. Relatively, the effect is most profound in the range of 500 mm $< a <$1000 mm, beyond which the influence is minor. Thus, if one is free to choose the diameter of circumcircle, it is advisable for him to keep it no greater than 500 mm to maximize the benefits of set-up in pile shaft capacity. From a different perspective, for one to improve the material efficiency, one effective way is thus to manipulate the diameters of circumcircle if a falls within the range from 500 m to 1000 m.

3.3.3 Influence of b

To explore the influence of the length of flat segments, eight different values of b spanning a practically typical range (i.e., 80 mm to 220 mm) are investigated. As illustrated in Fig. 23, the increase in b shortens the arc length of concave with subtle influence in the curve. In other words, the ratio of flat over cambered segment lengths get significantly increased. Furthermore, the cross-sectional area of XCC pile expands dramatically with the increase in b. Fig. 24 plots the variation of C_m against b. As with the case of a, C_m declines steadily as b increases. The declining tendency is most significant when b varies between 80mm and 180 mm, beyond which the influence is insignificant. Therefore, it is advisable to adjust, or decreases in more precise terms, b in such a range (80 mm – 180 mm) if needs arise to optimize the cross-sectional shape.

4. Conclusions

This paper reports a coupled effective stress analysis of XCC pile installation and consolidation, with particular emphasis on long-term stress conditions and set-up effects on pile shaft capacity. An in-housed developed large deformation finite element technique was first validated and subsequently applied to continually model the installation and consolidation phases of the XCC pile. The generation of excess pore pressure and alteration of stress states during the pile installation were then explored. Attention was paid to the distribution and magnitude of the effective normal stress at pile/soil interface, in particular its progress with consolidation. The influence of consolidation on the lateral earth pressure coefficient and the set-up effect on the XCC pile shaft resistance were investigated and quantified with care.

• It was suggested that the shaft resistance of XCC pile develops substantially with time. The post-installation consolidation brings in more capacity enhancements and therefore practical benefits than the conventional circular piles. The ultimate shaft resistance of XCC pile is 45% higher than that of the circular pile of the same cross-sectional area.

• The set-up effect can be incorporated into the design practices through β-method once the average stress improvement ratio over XCC pile shaft surface was determined.

• Additionally, parametric study gave practical advice on how to optimize of the cross-sectional shape of XCC piles for achieving economical designs. Since many practical benefits follows if set-up effects can be factored into design practices of XCC piles, the findings generated from this paper may be useful to promote wider application of XCC piles.

Acknowledgments

The authors wish to acknowledge the research funding provided by the National Natural Science Foundation of China (No. 51778091).

References

Abu-Farsakh, M., Rosti, F. and Souri, A. (2015), "Evaluating pile installation and subsequent thixotropic and consolidation effects on setup by numerical simulation for full-scale pi0le load tests", *Can. Geotech. J.*, **52**(11), 1734-1746. https:// doi.org/10.1139/cgj-2014-0470.

API (2014), Recommended Practice for Planning, Designing and Constructing Fixed Offshore Platforms-Working Stress Design, American Petroleum Institute, Washington, U.S.A.

Azari, B., Fatahi, B. and Khabbaz, H. (2015), "Numerical analysis of vertical drains accelerated consolidation considering combined soil disturbance and visco-plastic behaviour", *Geomech. Eng.*, **8**(2), 187-220. https://doi.org/10.12989/gae.2015.8.2.187.

Basu, P., Prezzi, M., Salgado, R. and Chakraborty, T. (2014), "Shaft Resistance and Setup Factors for Piles Jacked in Clay", *J. Geotech. Geoenviron. Eng.*, **140**(3), 04013026. https:// doi.org/10.1061/(ASCE)GT.1943-5606.0001018.

Cao, L., Teh, C. and Chang, M. (2001), "Undrained cavity expansion in modified Cam clay", *Geotechnique*, **51**(4): 323-334. https:// doi.org/10.1680/geot.51.4.323.39395.

Carter, J.P., Randolph, M.F. and Wroth, C.P. (1979), "Stress and pore pressure changes in clan during and after the expansion of a cylindrical cavity", *Int. J. Numer. Anal. Met.*, **3**(4): 305-322. https://doi.org/10.1002/nag.16100304 02.

Ceccato, F. and Simonini, P. (2017), "Numerical study of partially drained penetration and pore pressure dissipation in piezocone test", *Acta Geotechnica*, **12**(1): 1-15. https:// doi.org/10.1007/s11440-016-0448-6.

Ceccato, F., Beuth, L., Vermeer, P.A. and Simonini, P. (2016), "Two-phase Material Point Method applied to the study of cone penetration", *Comput. Geotech.*, **80**, 440-452. https:// doi.org/10.1016/j.compgeo.2016.03.003.

Dassault Systemes (2014), ABAQUS, Version 6.14 EF Documentation.

De Chaunac, H. and Holeyman, A. (2017), "Numerical analysis of the set-up around the shaft of a closed-ended pile driven in clay", *Geotechnique*, **68**(4), 332-344. https:// doi.org/10.1680/jgeot.16.P.229.

Ding, X., Luan, L., Liu, H., Zheng, C., Zhou, H. and Qin, H. (2020), "Performance of X-section cast-in-place concrete piles for highway constructions over soft clays", *Transport. Geotech.*, **22**: 100310. https:// doi.org/10.1016/j.trgeo.2019.100310.

Gavin, K., Gallagher, D., Doherty, P. and McCabe, B. (2010), "Field investigation of the effect of installation method on the shaft resistance of piles in clay", *Can. Geotech. J.*, **47**(7), 730-741. https:// doi.org/10.1139/t09-146.

Gong, W., Li, L., Zhang, S. and Li, J. (2020), "Long-term setup of a displacement pile in clay: An analytical framework", *Ocean Eng.*, **218**(11),10814. https:// doi.org/ 10.1016/j.oceaneng.2020.108143.

Haque, M.N. and Abu-Farsakh, M.Y. (2018), "Development of analytical models to estimate the increase in pile capacity with time (pile setup) from soil properties", *Acta Geotechnica*, **14**(3), 881-905. https:// doi.org/10.1007/s11440-018-0654-5.

Hyodo, J., Shiozaki, Y., Tamari, Y., Ozutsumi, O. and Ichii KJG. (2019), "Modeling of pile end Resistance considering the area of influence around the pile tip", *Geomech. Eng.*, **17**(3), 289-296. https://doi.org/10.12989/gae.2019.17.3.289.

Jaky, I. (1944), "The coefficient of earth pressure at rest", *J. Soc. Hung. Archit. Eng.* https://doi.org/10.1139/t94-091.

Karlsrud, K. (2014), "Ultimate shaft friction and load-displacement response of axially loaded piles in clay based on instrumented pile tests", *J. Geotech. Geoenviron. Eng.*, **140**(12). https://doi.org/10.1061/(ASCE)gt.1943-5606.0001170.

Khanmohammadi, M. and Fakharian, K. (2017), "Numerical modelling of pile installation and set-up effects on pile shaft capacity", *Int. J. Geotech. Eng.*, **13**(5), 484-498. https:// doi.org/10.1080/19386362.2017.1368185.

Kong, G.Q., Zhou, H., Ding, X.M. and Cao, Z.H. (2015), "Measuring effects of X-section pile installation in soft clay", *Proc. Inst. Civ. Eng. Geotech. Eng.*, **168**(4), 296-305. https:// doi.org/10.1680/geng.14.00048.

Li, L., Chen, H.H., Li, J.P. and Sun, D.A. (2021), "An elastoplastic solution to undrained expansion of a cylindrical cavity in SANICLAY under plane stress condition", *Comput. Geotech.*, **132**, 103990. https://doi.org/10.1016/j.compgeo.2020.103990.

Li, L., Gong, W. and Li, J. (2020), "Effects of clay creep on long-term load-carrying behaviors of bored piles: Aiming at reusing existing bored piles", *Int. J. Geomech.*, **20**(8), 04020132. https://doi.org/10.1061/(ASCE)gm.1943-5622.0001769.

Li, J. P., Li, L., Sun, D.A. and Gong, W.B. (2017a), "Time-dependent bearing capacity of jacked piles in K0 consolidated clay based on CPTU tests", *Chin. J. Geotech. Eng*, **39**(2), 193-200. https:// doi.org/0.11779/CJGE201702001.

Li, L., Li, J., Sun, D.A. and Gong, W. (2017b), "Analysis of time-dependent bearing capacity of a driven pile in clayey soils by total stress method", *Int. J. Geomech.*, **17**(7), 04016156. https://doi.org/10.1061/(ASCE)GM.1943-5622.0000860.

Li, L., Li, J., Sun, D. and Zhang, L. (2017c), "Time-dependent bearing capacity of a jacked pile: An analytical approach based on effective stress method", *Ocean Eng.*, **143**, 177-185. https:// doi.org/10.1016/j.oceaneng.2017.08.010.

Lim, Y.X., Tan, S. and Phoon, K. (2019), "Interpretation of horizontal permeability from piezocone dissipation tests in soft clays", *Comput. Geotech.*, **107**, 189-200. https:// doi.org/10.1016/j.compgeo.2018.12.001.

Liu, F., Yi, J. and Cheng, P. (2020), "Numerical simulation of set-up around shaft of XCC pile in clay", *Geomech. Eng.*, **21**(5), 489-501. https://doi.org/10.12989/gae.2020.21.5.489.

Liu, H., Zhou, H. and Kong, G. (2014), "XCC pile installation effect in soft soil ground: A simplified analytical model", *Comput. Geotech.*, **62**, 268-282. https:// doi.org/10.1016/j.compgeo.2014.07.007.

Lorenzo, R., Cunha, R.P.D., Neto, M.P.C. and Nairn, J.A. (2016), "umerical simulations of deep penetration problems using the material point method", *Geomech. Eng.*, **11**(1), 59-76. https://doi.org/10.12989/gae.2016.11.1.059

Lv, Y., Liu, H., Ding, X. and Kong, G. (2012), "Field tests on bearing characteristics of X-section pile composite foundation", *J. Perform. Constr. Fac.*, **26**(2), 180-189. https:// doi.org/10.1061/(ASCE)CF.1943-5509.0000247.

Lv, Y., Liu, H., Ng, C.W.W., Gunawan, A. and Ding, X. (2014a), "A modified analytical solution of soil stress distribution for XCC pile foundations", *Acta Geotechnica*, **9**(3), 529-546. https:// doi.org/10.1007/s11440-013-0280-1.

Lv, Y., Liu, H., Ng, C.W.W., Ding, X. and Gunawan, A. (2014b), "Three-dimensional numerical analysis of the stress transfer mechanism of XCC piled raft foundation", *Comput. Geotech.*, **55**, 365-377. https:// doi.org/10.1016/j.compgeo.2013.09.019.

Lv, Y., Ng, C.W.W., Lam, S.Y., Liu, H. and Ding, X. (2016), "Comparative study of Y-shaped and circular floating piles in consolidating clay", *Can. Geotech. J.*, **53**(9), 1483-1494. https:// doi.org/10.1139/cgj-2015-0634.

Lv, Y. and Zhang, D. (2018), "Geometrical effects on the load transfer mechanism of pile groups: three-dimensional numerical analysis", *Can. Geotech. J.*, **55**(5), 749-757. https:// doi.org/10.1139/cgj-2016-0518.

Mahmoodzadeh, H., Wang, D. and Randolph, M. (2015), "Interpretation of piezoball dissipation testing in clay", *Geotechnique*, **65**(10), 831-842. https://doi.org/10.1680/geot.14.P.213.

Peng, Y., Ding, X., Xiao, Y., Deng, X. and Deng, W. (2020), "Detailed amount of particle breakage in non-uniformly graded sands under one-dimensional compression", *Can. Geotech. J.*, **57**(8): 1239-1246. https://doi.org/10.1139/cgj-2019-0283.

Peng, Y., Liu, H., Li, C., Ding, X. and Deng, X. (2021), "The detailed particle breakage around the pile in coral sand", *Acta Geotechnica*, **16**, 1971-1981. https://doi.org/10.1007/s11440-020-01089-2.

Poulos, H.G. and Davis, E.H. (1980), *Pile Foundation Analysis and Design*, Wiley, Chichester, Sussex, England, U.K.

Rezania, M., Nezhad, M.M., Zanganeh, H., Castro, J. and Sivasithamparam, N. (2017), "Modeling pile setup in natural clay deposit considering soil anisotropy, structure, and creep effects: Case study", *Int. J. Geomech.*, **17**(3), 04016075. https://doi.org/10.1061/(ASCE)GM.1943-5622.0000774.

Rosti, F. (2016), "Numerical simulation of pile installation and following setup considering soil consolidation and thixotropy", Ph.D. Dissertation, Louisiana State University, Louisiana, U.S.A.

Silvestri, V. and Abousamra, G. (2012), "Analytical solution forundrained plane strain expansion of a cylindrical cavity in modified cam clay", *Geomech. Eng.*, **4**(1), 19-37. https://doi.org/10.12989/gae.2012.4.1.019.

Sun, G., Kong, G., Liu, H., and Amenuvor, A.C. (2017), "Vibration velocity of X-section cast-in-place concrete (XCC) pile–raft foundation model for a ballastless track", *Can. Geotech. J.*, **54**(9), 1340-1345. https:// doi.org/0.1139/cgj-2015-0623.

Tho, K.K., Leung, C.F., Chow, Y.K. and Swaddiwudhipong, S. (2012), "Eulerian finite-element technique for analysis of jack-up spudcan penetration", *Int. J. Geomech.*, **12**(1), 64-73. https:// doi.org/10.1061/(ASCE)GM.1943-5622.0000111.

Ullah, S.N., Hou, L.F., Satchithananthan, U., Chen, Z. and Gu, H. (2018), "A 3D RITSS approach for total stress and coupled-flow

large deformation problems using ABAQUS", *Comput*. *Geotech*., **99**, 203-215. https:// doi.org/0.1016/j.compgeo.2018.01.018.

Wang, Y., Li, L. and Li, J. (2021), "A similarity solution for undrained expansion of a cylindrical cavity in K_0-consolidated anisotropic soils", *Geomech*. *Eng*., **25**(4), 303-305. http://doi.org/10.12989/gae.2021.25.4.303.

Yi, J.T., Goh, S.H., Lee, F.H. and Randolph, M. (2012a), "A numerical study of cone penetration in fine-grained soils allowing for consolidation effects", *Geotechnique*, **62**(8), 707-719. https:// doi.org/10.1680/geot.8.P.155.

Yi, J.T., Lee, F.H., Goh, S.H., Zhang, X.Y. and Wu, J. (2012b), "Eulerian finite element analysis of excess pore pressure generated by spudcan installation into soft clay", *Comput*. *Geotech*., **42**, 157-170. https:// doi.org/0.1016/j.compgeo.2012.01.006.

Yi, J.T., Liu, F., Zhang, T.B, Yao, K. and Guo, Z. (2021), "A large deformation finite element investigation of pile group installations with consideration of intervening consolidation", *Appl*. *Ocean Res*., **112**, 102698. https://doi.org/10.1016/j.apor.2021.102698.

Yi, J.T., Zhao, B., Li, Y.P., Yang, Y., Lee, F.H., Goh, S.H., Zhang, X.Y. and Wu, J.F. (2014), "Post-installation pore-pressure changes around spudcan and long-term spudcan behaviour in soft clay", *Comput*. *Geotech*., **56**, 133-147. https:// doi.org/10.1016/j.compgeo.2013.11.007

Yi, J.T., Pan, Y.T., Qiu, Z.Z., Liu, F. and Zhang, L. (2020), "The post-installation consolidation settlement of jack-up spudcan foundations in clayey seabed soils", *Comput*. *Geotech*., **123**, 103611. https:// doi.org/10.1016/j.compgeo.2020.103611.

Zhang, D., Lv, Y., Liu, H., and Wang, M. (2015), "An analytical solution for load transfer mechanism of XCC pile foundations", *Comput*. *Geotech*., **67**, 223-228. https:// doi.org/10.1016/j.compgeo.2015.03.006.

Zhou, H., Liu, H., Randolph, M., Kong, G. and Cao, Z. (2017), "Experimental and analytical study of X-section cast-in-place concrete pile installation effect", *Int*. *J*. *Phys*. *Model*. *Geotech*., **17**(2), 103-121. https:// doi.org/10.1680/jphmg.15.00037.

Zhou, H., Yuan, J., Liu, H. and Kong, G. (2018), "Analytical model for evaluating XCC pile shaft capacity in soft soil by incorporating penetration effects", *Soils Found*., **58**(5), 1093-1112. https:// doi.org/10.1016/j.sandf.2018.04.005.

Zhou, H., Liu, H., Yuan, J. and Chu, J. (2019), "Numerical simulation of XCC pile penetration in undrained clay", *Comput*. *Geotech*., **106**, 18-41. https:// doi.org/10.1016/j.compgeo.2018.10.009.